

Revealing Molecular Mechanism of Nonmonotonic Relationship between Antifreeze Activity and Chain Length in Polyprolines

Wentao Yang, Yucong Liao, Zhaoru Sun*

School of Physical Science and Technology, ShanghaiTech University, Shanghai 201210, China

ABSTRACT: Ice recrystallization inhibition (IRI) activity of polymers generally increases with chain length. However, for polyproline (PPro), a highly potent cryoprotectant, the IRI activity varies nonmonotonically with the degree of polymerization (DP), i.e., DP=8 (P8) > DP=15 (P15) > DP=3 (P3). Herein, we employ molecular dynamics simulations to reveal the microscopic mechanism behind this nonmonotonic effect in PPro. Our findings indicate that the population of the PPII helix structure, which increases with DP, is not the primary reason for this effect. Instead, both single-molecule conformation and multi-molecule aggregation play critical roles. At the single-molecule level, PPro exhibits two types of thermodynamically stable conformations: linear (L) and coil (C), with the latter demonstrating enhanced IRI potency due to its stronger hydrophobicity and ice-binding capability. Notably, P8 has a higher content of the C conformation compared to P15, accounting for its superior IRI activity. Aligning with the conventional understandings, P3's lowest activity stems from its excessively small volume/coverage area on the ice surface. At the multi-molecule level, P15 shows a significantly higher tendency to aggregate than P8, which limits the ability of PPro molecules to fully spread at the ice-water interface and reduces their effective coverage of the ice surface, thereby diminishing its effectiveness. And P15's aggregation becomes significantly pronounced at high concentrations, amplifying the nonmonotonic effect. This work provides an atomistic insight into the nonmonotonic relationship between IRI activity and DP in PPro, offering valuable insights for the rational design of novel biocompatible antifreeze polymers.

KEYWORDS: polyproline; IRI; nonmonotonic effect; antifreeze mechanism; molecular dynamics simulation

1. INTRODUCTION

Cryopreservation is a critical technique for the long-term preservation of cells, tissues, and organs in biotechnology and biomedicine,¹⁻³ providing invaluable support for scientific research⁴⁻⁷ and clinical applications.⁸⁻¹⁰ The main challenge in the freeze-thaw process of cryopreservation is uncontrolled ice recrystallization, an Ostwald ripening process¹¹⁻¹³ in which larger ice crystals grow at the expense of smaller ones, leading to mechanical damage and osmotic shock, ultimately resulting in cell death.^{14,15} Fortunately, numerous antifreeze materials have been shown to effectively control ice crystal growth through the widely accepted adsorption-inhibition mechanisms, in which antifreeze agents bind to ice and prevent ice growth, thereby mitigating the detrimental effects of IR.¹⁶⁻³⁰ Among these materials,

polymers exhibit considerable ice recrystallization inhibition (IRI) activity, broad availability, low cost, and tunable properties (e.g., degree of polymerization (DP), monomer species, etc.),³¹⁻³³ which make them promising candidates for cryopreservation applications and have attracted tremendous research interest.³⁴⁻⁴⁰ Nevertheless, the rational design and development of optimized IRI-active polymers for practical industrial and medical applications remains an ongoing challenge in this field.⁴¹⁻⁴³

It is widely recognized that the IRI activity of polymers is directly correlated with their chain length or DP.^{13,31,44,45} Typically, the IRI activity increases monotonically with chain length/DP, as demonstrated in a variety of materials including poly(vinyl alcohol) (PVA),¹³ poly(L-alanine-co-L-lysine),³⁴ nanocelluloses,⁴⁶ and others.⁴⁷⁻⁵⁰ This phenomenon can be explained by a well-established mechanism that the longer chain provides more ice-binding sites, along with a larger effective volume and increased contact area with the ice surface. This enhances the ice-binding strength and prevents the polymer being engulfed by the advancing ice front, thereby improving IRI performance.^{41,51}

However, certain polymers, such as polyproline (PPro),⁵² zwitterionic poly(carboxybetaine methacrylate),⁵³ thymine oligomers,⁵⁴ exhibit an intriguing yet poorly understood nonmonotonic relationship between IRI activity and chain length or DP. In this case, the IRI activity initially increases but then declines as the chain length increases, with the highest activity observed at an intermediate chain length. Among these, PPro is the simplest and most representative system of this phenomenon, demonstrating excellent biocompatibility and significant potential for practical applications in cryopreservation compared to other polymers.^{33,52} Experimental studies⁵² have shown that PPro with DP=8 (denoted as P8) exhibits the highest activity, outperforming both shorter (i.e., P3) and longer (i.e., P15) PPro chains. This suggests that the mechanism underlying the relationship between IRI activity and chain length is more complex in PPro than in conventional polymers such as PVA.⁵¹ Uncovering this mechanism is essential to deepen our understanding of polymer IRI activity and for the rational design of more effective and biocompatible polymer-based antifreeze agents.

One interpretation of this nonmonotonic phenomenon is that PPro inhibits ice growth by binding to ice through its methylene (-CH₂) groups within the linear amphipathic polyproline II (PPII) helix structure.⁵⁵ Preservation of this unique PPII helix dictates its IRI activity.³³ For example, Wang et al.⁵² hypothesized that P8's superior activity is attributed to its perfect PPII helix structure, which facilitates its binding to the ice surface. In contrast, P3 is too short to form the PPII structure, and P15 primarily adopts the coiled conformation with a reduced PPII content. However, recent findings by Rojas et al.⁵⁶ challenge this view. Their circular dichroism (CD) experiments revealed that the PPII content of PPro increases with DP, with P8 exhibiting a more disordered structure compared to P15. This suggests that the PPII content alone cannot explain this nonmonotonic effect in PPro. Additionally, recent study⁵³ on another polymer system, zwitterionic poly(carboxybetaine methacrylate), suggested that the nonmonotonic effect originates from the degree of molecular extension, which directly influences the contact area and determines its IRI activity. Therefore, a comprehensive investigation of the molecular conformation of PPro and its impact on IRI activity at the atomic level is imperative for a complete understanding of the nonmonotonic effect.

In addition to the debates on single-molecule conformation, polymer aggregation has also been proposed to influence the IRI activity of PPro. For example, Judge et al.⁵⁷ recently reported that high molecular weight PPros (DP > 200) can aggregate at room temperature and suggested that this aggregation may contribute to its IRI activity. However,

the impact of aggregation on IRI activity varies across different materials.⁵⁸⁻⁶³ For instance, in saffron molecules⁵⁸ and self-assembled peptides,⁵⁹⁻⁶¹ aggregation has been shown to enhance their IRI activity by forming ordered structures that resemble ice-binding surfaces of antifreeze proteins. In contrast, for polymers such as isotactic PVA,⁶² tamarind seed polysaccharides,⁴⁴ and nanocelluloses,^{63,64} aggregation has been associated with reduced IRI activity, due to diminished surface coverage on the ice surface. Therefore, although aggregation has been observed in PPro systems,^{57,65,66} its specific role in IRI activity, particularly in contributing to the nonmonotonic effect, requires further investigation.

In this work, we use all-atom molecular dynamics (MD) simulations to reveal the molecular mechanism underlying the nonmonotonic relationship between IRI activity and chain length/DP in PPro (i.e., P8 > P3 > P15) by systematically investigating the influences of single-molecule conformation and multi-molecule aggregation. At the single-molecule level, we first explore the conformational free energy landscapes of PPros through metadynamics simulations, and find that PPro adopts two types of energy-favorable conformations: linear (L) and coil (C), with P8 exhibits a higher content of the C conformation compared to P15. Subsequently, we evaluate their IRI activity through MD simulations, showing that the overall IRI performance decreased in the order P8 > P15 > P3, aligning with experimental studies.⁵² Notably, the C conformation exhibit greater effectiveness in inhibiting ice growth compared to the L conformation. We demonstrate that P8's superior IRI activity arises from its sufficient coverage area on the ice surface, which prevents its engulfment by the advancing ice front, and its higher proportion of the C conformation, which possesses enhanced molecular hydrophobicity and greater ice-binding capability that facilitate the binding of P8C to the ice surface. At the multi-molecule level, we investigate the aggregation tendencies of PPro across various DPs and find that P15 exhibits strongest tendency to aggregate. However, P15 aggregates into disordered three-dimensional (3D) structure, which limits its ability to fully spread at the ice-water interface and reduces its effective surface coverage area on ice, thereby further reducing its IRI performance. We also show that P15's aggregation becomes significantly pronounced at high concentrations, amplifying the nonmonotonic effect. By clarifying this molecular mechanism, our findings will facilitate the rational design of more effective polymer-based IR inhibitors.

2. RESULTS AND DISCUSSION

2.1. PPII helix structure is not the primary reason for the nonmonotonic effect in PPro, but the linear/coil conformational preference. It has been established that the conformation of antifreeze agents significantly influences their IRI activity.^{20,51,52,67} Therefore, we first calculate the conformational free energy landscapes of PPros in solution with DP = 3, 8, 15 (denoted as P3, P8, and P15, respectively) through well-tempered metadynamics simulations (see Section 4.2). The radius of gyration (R_g) is chosen as the collective variable to bias, where lower R_g value indicates a more compact PPro chain. As illustrated in Figure 1a, all PPro chains adopt two types of energetically favorable conformations: compact coil (C) and extended linear (L) forms (labeled as PnC and PnL, with n representing the DP). This observation is consistent with previous experimental results.^{68,69} Furthermore, the two conformations of P3 exhibit negligible differences, particularly in surface area and volume (not shown), and thus will not differentiated them in subsequent simulations.

With a further examination of L and C conformations in P8 and P15, it supports that the C conformation originates from the interspersing of the cis/trans isomers in PPro.⁶⁹ Specifically, P8 shows a slightly higher energy barrier (L to C ~ 0.8 kJ/mol) compared P15, indicating a greater flexibility in P15, consistent with previous findings.⁶⁹ Furthermore, the free energy difference between the C and L conformation in P8 is about 1.5 kJ/mol lower than that in P15, suggesting that the C conformation in P8 is more thermodynamically stable than P15. The population ratio between the C and L conformations of P8 and P15 can be thermodynamically estimated as $p(L)/p(C) = \exp([G_C - G_L]/k_B T) = \exp(\Delta G_{CL}/k_B T)$, where ΔG_{CL} represents the free energy difference between two conformations, k_B is Boltzmann constant, and T is absolute temperature. A smaller free energy difference (ΔG_{CL}) results in a higher content of C conformation. Therefore, the C conformation content in P8 is expected to be approximately twice that of the P15 at the same molar concentration.

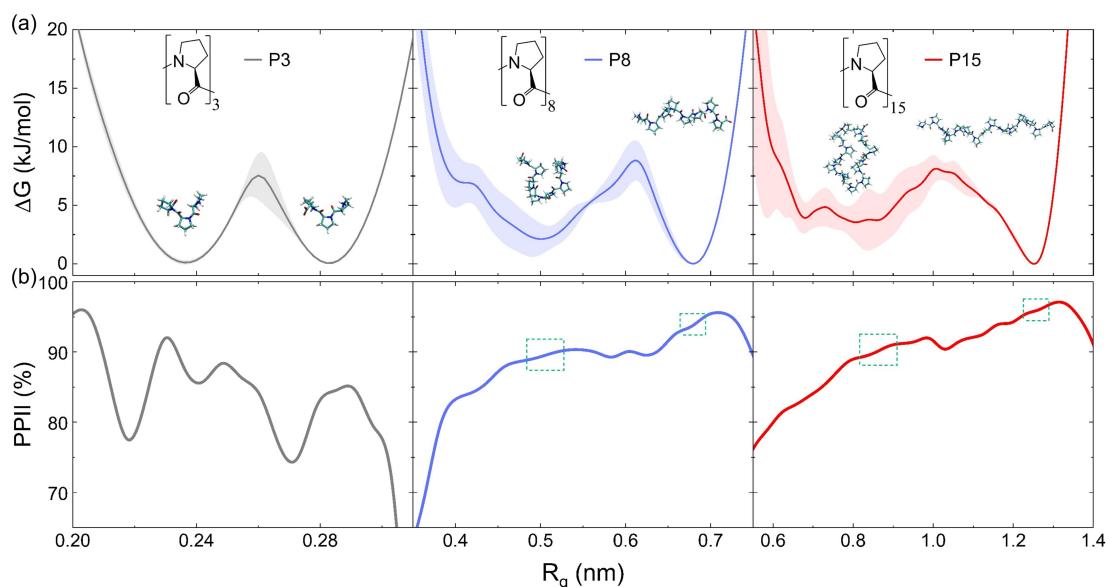


Figure 1. Conformational landscapes of PPros in solution at 300 K. (a) Gibbs free energy (ΔG) profile as a function of the radius of gyration (R_g) for P3 (light gray), P8 (blue), and P15 (red). PPro are relatively rigid molecules that adopt two thermodynamically stable conformations: the linear (L) and coil (C) forms, which are separated by energy barriers approximately 2-3 times the magnitude of thermal fluctuations at room temperature ($k_B T \approx 2.5$ kJ/mol). The shaded region represents the standard error associated with our estimate of ΔG . (b) Population of the PPII helix as a function of R_g , colors as in (a). Dotted green squares mark the location of the R_g with the thermodynamically stable conformations.

Figure 1b shows the population of the PPII helix structure as a function of R_g for PPros. Notably, the PPII helix is the dominant structure in both P8 and P15, with PPII content exceeding 90% even within the compact C conformation. And the population becomes more pronounced with increasing R_g . In contrast, P3 displays a more disordered and less defined secondary structure, with no clear correlation between PPII population and R_g . However, even in the case of P3, the PPII helix remains the dominant structure with a population of more than 60%. Furthermore, we calculate the total PPII content across various DPs and find that it follows the order P3 ($\sim 63\%$) < P8 ($\sim 80\%$) < P15 ($\sim 87\%$), indicating that the PPII helix secondary structure becomes more clearly defined with increasing DP, consistent with recent

experimental observations.⁵⁶ Based on these results, we speculate that the dominant PPII helix structure is an intrinsic feature of PPro and is not the primary driver of the nonmonotonic effect; instead, the variation in conformational preferences is the underlying cause of this phenomenon.

2.2. Impact of PPro with different DPs and conformations on ice growth. To investigate the influence of PPro with varying DP and conformations—specially P8 and P15 in both C and L forms, as well as P3—on the ice inhibition process, as well as P3, on the ice inhibition process, we conduct a series of independent MD simulations with the polymers being presented at the ice/water interface of the ice prismatic plane at 265 K (simulation details are provided in Section 4.1). As shown in Figure 2a, it is evident that the presence of PPro significantly inhibits ice growth, with the ranking of the inhibition efficacy of PPro with representative conformations as follows: P8C > P15C > P8L ≈ P15L > P3. Considering the results of our free energy calculations, which indicates that P8 possesses a higher content of the C conformation compared to P15, we conclude that the overall IRI performance should follow the order P8 > P15 > P3. This conclusion aligns well with the nonmonotonic experimental results.⁵²

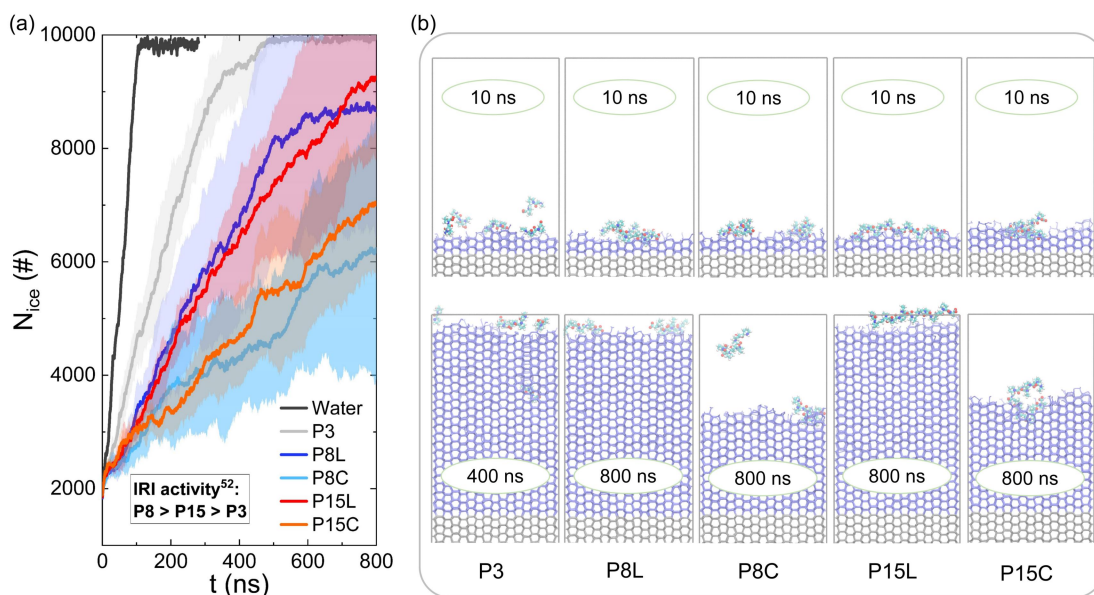


Figure 2. Ice growth inhibition ability of PPro with different DPs (3,8,15) and conformations (L and C). (a) Time evolution of the number of ice molecules of different simulation systems, including P3 (gray line), P8L (blue line), P8C (light blue line), P15L (red line), P15C (orange line), and a control without PPro (black line). Data represent averages from five independent simulations, with error bars indicated as shaded regions. (b) Representative snapshots of ice growth in the presence of PPro.

Interestingly, we observe that PPro in the C conformation exhibits a significantly stronger ice growth inhibition ability compared to its L conformation (Figure 2a), even though the latter has a higher population of PPII helix structure. Therefore, we argue that the conformational preference of PPro, rather than the PPII content, is crucial for the nonmonotonic relationship between its IRI activity and chain length.

Figure 2b shows the representative snapshots of ice growth in the presence of PPro in our MD simulations. Not surprisingly, P3 is too small and tends to be easily displaced from the ice-water interface or rapidly overgrown by the

advancing ice front (Figure 2 and Movie S1). This behavior results in minimal steric hindrance to ice growth and consequently low IRI activity. In contrast, P8 and P15 in the C conformation can adhere to the ice surface for extended periods (>400 ns), with the curved regions of their chains inserted into the ice surface without being engulfed, thus demonstrating significant inhibition of ice growth (Figure 2, Movies S2,S3). However, while P15L and P8L can remain at the ice-water interface, they are less effective at inhibiting the growth of ice front (Figure 2, Movies S4,S5), exhibiting relatively weak inhibition capabilities. Additionally, it is observed that all PPro chains exhibit reversible binding to ice, with the order of reversibility follows: P8C < P15C < P8L < P15L < P3, which is consistent with their inhibition abilities. These results suggest that the adoption of the C conformation is crucial for the IRI performance of PPro, significantly enhancing its ice-binding capability.

2.3. The IRI activity of PPro: hydrophobicity, ice-binding capability, and engulfment resistance. The ice growth and recrystallization process of antifreeze molecules involves three critical steps. First, the antifreeze molecule has to diffuse readily from the bulk aqueous phase to the ice-water interface and subsequently remain there.⁷⁰ Second, the antifreeze molecule must effectively attach to and bind tightly with the ice surface.⁴¹ Finally, the antifreeze molecule bound to the ice surface must resist engulfment by the growing ice front.⁷¹ For PPro, the first step is typically determined by hydrophobicity, the second step by ice-binding capability, and the last step by engulfment resistance ability. In the following section, we will systematically elaborate on how these factors influence the IRI performance of P3, P8, and P15.

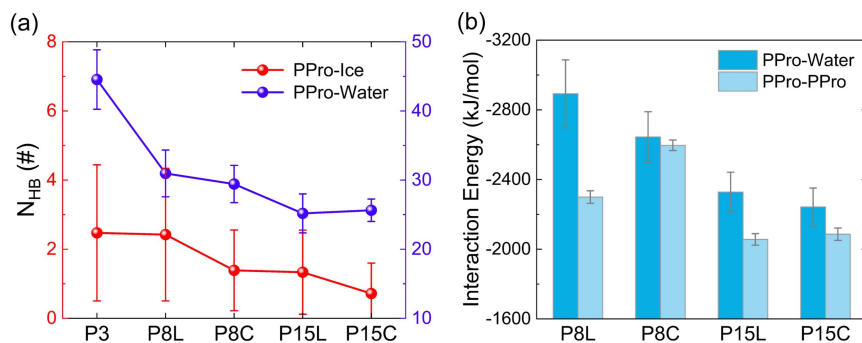


Figure 3. Interaction analysis of PPro-water, PPro-ice and PPro-PPro. (a) Total number of hydrogen bonds formed by PPro with ice (blue line) or water (red line). (b) Interaction energies between PPro (DP=8, 15) and water (blue) or PPro (light blue).

In the first step, the ice surface acts as a hydrophobic wall,⁷² where more hydrophobic (or less hydrophilic) PPro molecules are more likely to migrate to and remain at the ice-water interface. Our simulations reveal that most of the P3 chains predominantly remain in the liquid phase (Movie S1), while P8 and P15 remain continuously at the ice-water interface (Movies S2-S5). This observation indicates that the first step is particularly unfavorable for P3 due to its insufficient hydrophobicity.

In order to quantitatively assess the hydrophilicity of these PPro chains, we calculate the total number of hydrogen bonds formed between PPro molecules and water/ice in ice inhibition simulations, as shown in Figure 3a. The total number of hydrogen bonds formed between PPro and water follows the order P3 > P8L > P8C > P15L > P15C (Figure 3a), indicating that shorter PPro chains are more hydrophilic. This explains why P3 readily dissociates from the ice-water interface and dissolves in the aqueous phase, while P8 and P15 are more likely to remain at the interface.

Consistent with recent studies,⁵⁵ there are almost no direct hydrogen bonds formed between PPro and ice. This suggests that the retention of PPro at the ice-water interface is not driven by enthalpic contributions from hydrogen bonding, but rather by hydrophobic entropy from the partial desolvation of the hydrophobic $-\text{CH}_2$ groups. We speculate that the hydrophobic effect of the $-\text{CH}_2$ groups facilitates the migration of PPro molecules to and their retention at the ice-water interface, while the hydrogen-bonding groups primarily contribute to the solubility of PPro.

To explore how the L and C conformations of P8 and P15 affect the first diffusion step, we calculate the interaction energies between PPro and PPro/water. As shown in Figure 3b, PPro in the C conformation exhibits weaker interaction energy with water compared to the L conformation, indicating that the latter is more hydrophilic. Conversely, the C conformation demonstrates greater hydrophobicity, facilitating its migration to and retention at the ice-water interface. Furthermore, when comparing the interactions between PPro molecules, we find that the C conformation exhibits a stronger interaction, making it more rigid and less prone to deformation during diffusion towards the interface (Figure 3a). This suggests that the PPro in the C conformation incurs a lower configurational entropy cost throughout the diffusion process and subsequent steps, thereby promoting its rapid migration to and stabilization at the ice-water interface.

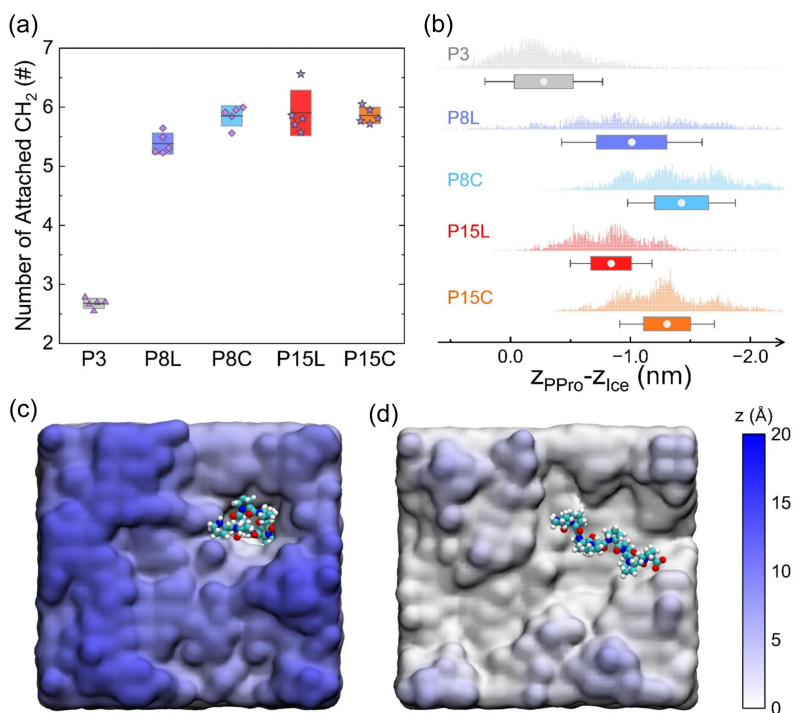


Figure 4. Binding states of PPro to the ice surface. (a) Average number of methylene ($-\text{CH}_2$) groups per PPro molecule attached to the ice surface, with data averaged over for five independent simulations (color scheme as in Figure 2a). (b) Embedded depth of PPro at the ice surface. (c-d) Representative binding states and configurations of P8C (c) and P8L (d), where the colors of the ice surface correspond to the height of the z -axis and the bottom atom of PPro is chosen as the reference point ($z=0$). PPro molecules that stay away from the ice surface (unbound) are not shown. Additional PPro chains are shown in Figure S2. P8C forms the deepest trap on ice surfaces and binds most strongly to ice.

In the second step, the ice affinity of the PPro molecule allows it to attach to the ice surface, while robust ice-binding strength ensures firm adsorption and prevents detachment. To evaluate the ice affinity of PPros with various DP and conformations, we calculate the average number (N_{CH_2}) of the $-\text{CH}_2$ groups attached to ice for each PPro molecule (Figure 4a). The results show that the N_{CH_2} increases rapidly with DP and reaches a plateau around 6 when DP=8, suggesting that P8 achieves sufficient ice affinity. Notably, the N_{CH_2} of P15 does not significantly exceed that of P8, indicating that only a fraction of the proline repeats in P15 effectively attach to the ice surface, even for the extended L conformation (P15L). This implies that excessively long chains, regardless of conformation, are not conducive to a perfect fit on the ice surface, since the surface of ice front is not completely flat. In contrast, the low N_{CH_2} value of P3 (~ 2.6) reflects its weak ice affinity, attributable to the low hydrophobic dehydration energy of its $-\text{CH}_2$ groups (estimated to be less than 6 kJ/mol from previous studies⁷²), leading to the majority of P3 molecules detaching from the ice surface. Furthermore, PPro in the C conformation has a slightly higher N_{CH_2} value compared to the L conformation, indicating that the C conformation is more effective for attachment to ice surface and possesses a greater ice affinity. In light of these results, we conclude that P8 demonstrates sufficient ice affinity to adhere to the ice surface, with the C conformation showing superior performance in this regard.

Nevertheless, high ice affinity (i.e., N_{CH_2}) is necessary but not sufficient for PPro to effectively inhibit ice growth, as demonstrated by P8L and P15L. To further analyze the ice-binding strength, we assess the embedded depth of PPro on the ice surface during binding but without complete engulfment. As shown in Figure 4b, more negative values of the horizontal axis indicate stronger ice-binding strength. It is observed that P8C exhibits the most significant embedded depth (Figure 4b), acting as a wedge inserted into the ice surface without being engulfed by ice, which lead to the formation of obvious folds and roughness on the ice surface (Figures 4c and S2f-j). This indicates that the ice surface adsorbed by P8C generates a larger curvature, thereby effectively inhibiting ice growth through the Gibbs-Thomson effect. Similarly, P15C is also clearly embedded in the ice surface, as evidenced by the formation of significant folds (Figure S2e). However, P8L and P15L show only minimal embedding and produce slight surface folding (Figures 4b and S2f-j), which can be attributed to their continual attachment to and detachment from the ice surface. This suggests that PPro in the L conformation has a relatively weak ice-binding strength compared to that in the C conformation. As expected, P3 molecules exhibits only partial attachment to the ice and show minimal embedded depth, resulting in a very flat ice surface (Figure S2a,f) with limited contributions to the Gibbs-Thomson effect. In light of these results, we conclude that the superior performance of the P8 (particularly in the C conformation) compared to P15, is attributed to its greater ice-binding capability, as determined by both ice affinity and embedded depth.

In the final step, PPro molecule bound to ice acts like a "sand forest", creating steric hindrance at the advancing ice front without being engulfed, thereby inhibiting ice growth. In this context, it is evident that PPro effectively resists engulfment by the ice front when its effective coverage area on the ice surface exceeds 3.3 nm² (see Figure 5). For example, P8C and P15C are rarely engulfed during our ice growth inhibition simulation (Figure S2c, e). In contrast, when P8L and P15L attach in a parallel orientation to the advancing ice front, they are more prone to being engulfed due to their inadequate coverage area, which ultimately leads to the failure of ice growth inhibition (Figure S3). Therefore, we conclude that the effective coverage area of PPro molecules on the ice surface determines their ability to resist.

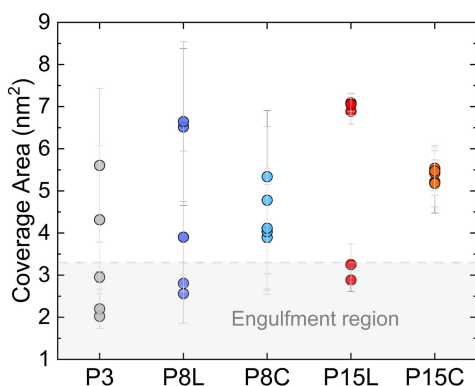


Figure 5. Average coverage area of PPro on the ice surface. Colors correspond to those used as in Figure 2a. Data points for each PPro molecule are obtained from five independent simulations, with the total ice surface area of approximately 32 nm².

Unlike PVA, where the effective volume and contact area with the ice surface determine its IRI activity,⁵¹ the origins of PPro's IRI activity are notably more complex. This complexity primarily stems from the fact that PPro interacts with ice primarily through hydrophobic interactions, whereas PVA relies on direct hydrogen bonding. In light of the above analyses, we conclude that the superior IRI activity of P8 is attributed to its elevated content of the C conformation. To elaborate, the enhanced hydrophobicity of P8C promotes its migration from the aqueous phase to the ice-water interface. Additionally, P8C exhibits an ice affinity comparable to that of P15 while achieving the deepest embedding depth at the ice surface, thereby strengthening its ice-binding capability. Moreover, the adequate surface coverage area of P8C effectively prevents its engulfment by the advancing ice front.

2.4. Aggregation and its impact on the IRI performance of PPro. Previous experimental studies have indicated that aggregation/assembly significantly influences the IRI activity of polymers.⁵⁷⁻⁶⁴ To explore the impact of PPro aggregation on the nonmonotonic effect, we first investigate the aggregation tendency of PPro through WTMetaD simulations (see Section 4.2), employing the coordination number (CN) as the collective variable to bias. A larger CN value indicates a higher degree of aggregation. As expected, both L and C conformations of PPro are effectively captured in the WTMetaD simulations. Figure 5a presents the energy landscape for the aggregation (dimer) of PPro with DP=3, 8, and 15 at a low concentration (~10 mg/mL). The horizontal axis is scaled by the value corresponding to the aggregation state (CN_A), with the raw data presented in Figure S4. We find that P3 and P8 do not exhibit discernible energy minima in the aggregated state, whereas P15 reveals a significantly high aggregation energy barrier despite showing a pronounced energy minimum at the aggregated state ($CN/CN_A = 1.0$). This finding suggests that aggregation is exceedingly improbable for these PPro chains at this low concentration.

Similarly, Figure 5b depicts the aggregational free energy landscape of PPro at a high concentration, reflecting the IRI experimental condition (40 mg/mL).^{52,55} The nonzero minimum CN value arises from the coordination of intramolecular adjacent atoms. Both dispersed (D) and aggregated (A) states are explored across all DPs, with representative configurations shown in Figure 5c-g. Notably, P3 and P8 exhibit high free energies (> 16 kJ/mol) in the aggregated state, accompanied by substantial energy barriers (> 18 kJ/mol) to aggregation, indicating a strong tendency to remain in the dispersed state. In contrast, P15 shows a relatively lower free energy of just below ~3 kJ/mol in the

aggregated state, with a significantly smaller aggregation energy barrier (~ 10 kJ/mol). This finding indicates that P15 exhibits a notable tendency to aggregate at high concentrations.

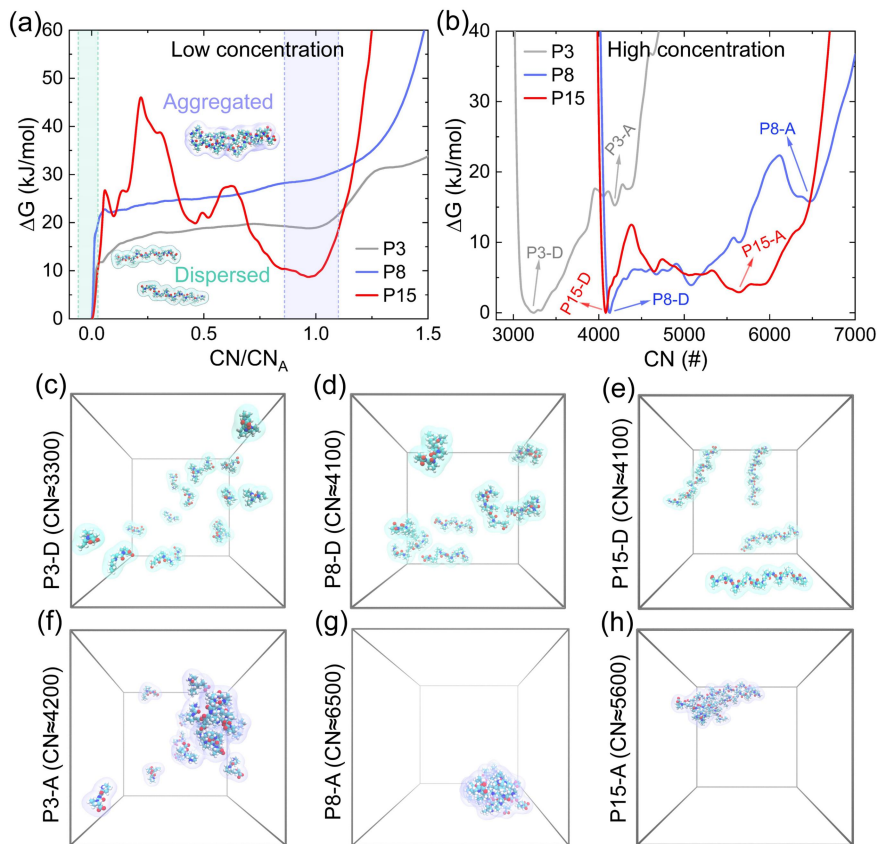


Figure 6. Aggregation tendencies of PPros. (a) Free energy landscape of dimer formation for PPros (DP=3,8,15) at low concentrations (~ 10 mg/mL), using CN as the collective variable to bias. The horizontal axis is scaled to their represent aggregation coordination number (CN_A), with raw data available in Figure S4. (b) Gibbs free energy (ΔG) profile as a function of CN obtained from WTMetaD simulations at high concentrations (~ 40 mg/mL). (c-e) Representative dispersed configurations of P3, P8, and P15, respectively, and (f-h) representative aggregated configurations of P3, P8, and P15 from the WTMetaD simulations of (b).

Further examination of P15 aggregation reveals that it typically forms disordered, amorphous 3D structures (Figure 5f-h), consistent with previous experimental observations.^{57,65} Regarding the metastable states ($CN \approx 5100$ for P8 and $CN \approx 4900$ for P15), which primarily involve dimer formation (Figure S5), they impact on PPro's IRI activity is expected to be negligible due to their high instability and susceptibility to disruption by advancing ice front.

To investigate the impact of P15's disordered aggregation on its IRI performance, we perform ice inhibition simulations for P15 in both aggregated and dispersed states, as shown in Figure 7. Notably, aggregated P15 exhibits a reduced ability to inhibit ice growth and is gradually overgrown by the advancing ice front. In contrast, dispersed P15 effectively inhibits ice growth due to its enhanced coverage on the ice surface. These findings suggest that P15's disordered aggregation limits its ability to fully spread at the ice-water interface, thereby reducing its effective coverage area on the ice surface and leading to the failure in inhibiting ice growth. This finding aligns well with the previous experimental results, which highlighted a more pronounced difference in IRI activity between P8 and P15 at

high concentrations.⁵⁰ Consequently, we conclude that the aggregation P15 at elevated concentrations significantly diminishes its IRI performance, thereby amplifying the nonmonotonic effect.

In addition, we find that there are almost no intermolecular hydrogen bonds formed in the P15 aggregations (Figure S6), indicating that hydrophobic interactions primarily drive the aggregation. As DP increases, the aggregation phenomenon becomes more pronounced due to enhanced hydrophobicity. This explains the experimental observation that PPros with DP > 100 aggregate at much lower concentrations (2 mg/mL).⁵⁷ For high molecular weight PPros (DP > 100), their sufficiently strong hydrophobicity gives rise to a comparable aggregation tendency. In this context, aggregation exerts a similar influence on their IRI activity, resulting in a trend where IRI activities increase with DP, as observed in experimental study.⁵⁷

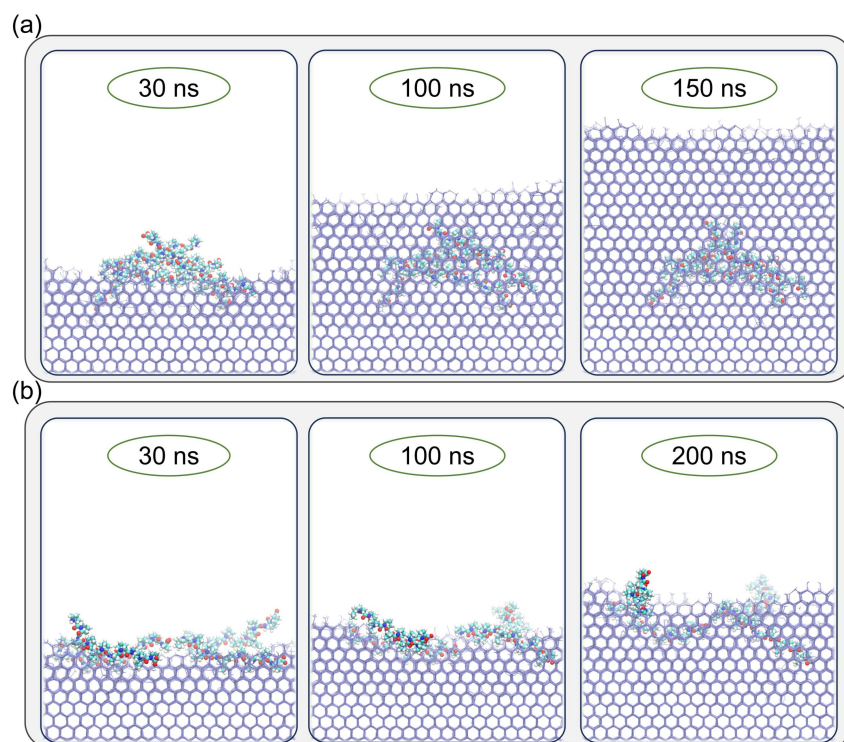


Figure 7. Impact of aggregation on ice growth inhibition of P15. (a) Aggregated P15 molecules are engulfed by the advancing ice front. (b) Dispersed P15 molecules effectively inhibit ice growth.

3. CONCLUSIONS AND OUTLOOK

In this work, we employ all-atom molecular dynamics simulations to elucidate the microscopic mechanism underlying the anomalous nonmonotonic variation of IRI activity in PPro with various DP. Our simulations indicate that the overall IRI performance decreases in the order P8 > P15 > P3, aligning with experimental observations.⁵² Notably, we find that the PPII helix structure is not the primary reason for this nonmonotonic effect, because its content increases with DP. Instead, both single-molecule conformation and multi-molecule aggregation are crucial. To our knowledge, this is the first report to provide comprehensive atomistic insights into the nonmonotonic effect from molecular simulations.

At the single-molecule level, our simulations indicate that molecular hydrophobicity, ice-binding capability, and engulfment resistance ability collectively dictate the IRI potency of the polymer. Consistent with conventional understandings, the minimal activity of the short PPro chains (e.g., P3) stems from its weak hydrophobicity and excessively small volume/effective coverage area on the ice surface. In contrast, the medium-length PPro chains (e.g., P8) already possess sufficient molecular volume and coverage area on the ice surface to effectively resist the engulfment by ice. Furthermore, our metadynamics calculations reveal that PPro adopts two thermodynamically stable conformations: linear (L) and coil (C). The latter displays greater IRI performance due to its superior hydrophobicity and ice-binding capability. Notably, P8 contains a higher proportion of the C conformation compared to P15 at the same proline monomer concentration, which directly accounts for its superior IRI activity.

At the multi-molecule level, our results demonstrate that the longish PPro chains (e.g., P15) tend to aggregate at high concentrations, whereas P8 remains in a dispersed state. This aggregation in P15 limits its ability to fully spread at the ice-water interface, thereby reducing its effective coverage on the ice surface. Therefore, we conclude that the aggregation of P15 diminishes its IRI activity, amplifying the nonmonotonic effect at high concentrations.

In light of our findings which demonstrate that the nonmonotonic effect observed in PPro originates from the combinational contribution of single-molecule conformation and multi-molecular aggregation, we propose a robust framework for elucidating the non-monotonic effect observed in other polymers. For instance, in thymine oligomers,⁵⁴ conformational preference is critical, with the strongest IRI activity occurring at DP = 20 due to its optimal coiled conformation and suitable volume for engulfment resistance and ice-binding property. Similarly, the nonmonotonic effect observed in zwitterionic poly(carboxybetaine methacrylate) (PCBMA)⁵³ can be attributed to variations in conformational preferences across different DPs. Specifically, PCBMA with a DP of 30 exhibits a more expanded conformation, enhancing its resistance to engulfment while maintaining comparable ice-binding strength compared to PCBMA with larger DPs, thus demonstrating elevated IRI activity. Moreover, tamarind seed polysaccharides (TSPs),⁴⁴ which bind to ice through hydrogen bonding, show the highest antifreeze activity at intermediate molecular weights. As molecular weight increases, TSPs initially benefit from enhanced binding and resistance to engulfment due to increased volume and hydrogen bond formation with the ice surface. However, beyond a certain threshold, aggregation reduces the effective surface coverage, consequently lower its IRI activity. We conclude that both the single-molecule conformation and multi-molecular aggregation are necessary to be considered in IRI activity, although their contributions vary across different polymer systems.

Our work provides several guidelines for the rational design of high-performance ice inhibition polymers: (i) Excellent solubility in aqueous solutions; (ii) Sufficient molecular weight/volume to prevent the engulfment by ice; (iii) Appropriate hydrophobicity to facilitate migration to the ice-water interface from aqueous phase and attachment to the ice surface; (iv) A higher content of coiled conformation, which generally provides greater ice-binding capability; (v) Ability to remain fully dispersed or to aggregate into ordered structures which exposing surfaces similar to the ice-binding surface of AFPs in aqueous solution. Overall, this study elucidates the atomistic details of the nonmonotonic relationships between IRI activity and chain length/DP for polymers, offering valuable guidance for the rational design of novel antifreeze agents for medical, industrial, and agricultural applications.

4. METHODS

4.1. Molecular dynamics simulations. All molecular dynamics simulations were carried out by GROMACS 2020.7 packages⁷³ using the all-atomistic CHARMM36 forcefield⁷⁴ and the TIP4P/Ice water model.⁷⁵ The melting temperature of ice Ih in this water model is 270 K, in good agreement with the experimental value of 273.15 K.⁷⁶ The cutoffs for the van der Waals and coulombic interactions were set to 1.2 nm, and long-range electrostatic interactions were evaluated with the particle-mesh Ewald (PME) algorithm.⁷⁷ The LINCS algorithm⁷⁸ was employed to constrain the covalent chemical bonds including hydrogen atoms. The equations of motion were integrated using the leapfrog method with a time step of 2 fs across all simulations. Periodic boundary conditions were applied in three directions. The temperature T and pressure P for production runs were controlled with the Nosé–Hoover thermostat^{79,80} and Parrinello-Rahman barostat,⁸¹ with time constants of 0.5 and 2.0 ps, respectively. The pressure was set to 1 atm in all NPT-MD simulations.

To investigate the ice growth inhibition ability of PPro with DP=3, 8, and 15, the polymers in stable conformations (obtained from metadynamics simulations, see Section 4.2) were placed on top of four layers of hexagonal ice generated from the Genice program.⁸² The system was then solvated with ~10000 water molecules, as previous experiments have reported that the PPro exhibit IRI activity at concentrations of 10 mg/mL.^{33,52} The PPro molecules (P3, P8L, P8C, P15L, and P15C) were positioned approximately 1.0 nm above the primary prismatic plane of the ice crystal (see Figure S1), maintaining consistent proline monomer concentrations across all DPs, using 5, 2, and 1 chains for DP = 3, 8, and 15, respectively. The initial dimensions of the simulation box were $5.87 \times 5.42 \times 12.00$ nm³. All the initial ice were constrained by a harmonic potential with a force constant of 1000 kJ mol⁻¹ nm⁻². Five independent simulations were conducted for each PPro (P3, P8L, P8C, P15L and P15C) with different backbone orientations parallel to the ice surface. First, the energy minimization has been conducted using the steepest descent method with a maximum force tolerance of 1000 kJ mol⁻¹ nm⁻¹. Then, the system was subsequently equilibrated at 275 K for 500 ps with NPT-MD simulation, followed by pre-equilibration at 265 K under the same ensemble. Finally, an 800 ns production NPT-MD run at 265 K was performed to monitor the ice growth inhibition activity, with restraints applied to a ~1 nm layer of water molecules below the ice slab to prevent initial ice growth in the down-ward direction.

To address the impact of P15 aggregation on ice growth, ice growth inhibition simulations were performed using four P15 chains in both aggregated and dispersed states, as obtained from metadynamics simulations (see Section 4.2) The initial simulation box dimensions were $11.75 \times 11.77 \times 12.00$ nm³, containing approximately 46,000 water molecules and four layers of hexagonal ice.

4.2. Metadynamics simulations. The well-tempered metadynamics (WTMetaD),⁸³ a powerful and well-established enhanced sampling technique which drives the system to explore the entire free energy surface with respect to selected collective variables (CVs), was employed to investigate the conformational space of PPro and its aggregation property in solution. All metadynamics simulations were performed using PLUMED 2.8^{84,85} plugin integrated with GROMACS 2020.7.⁷³

Prior to the WTMetaD simulations, a polyproline (DP=3,8,15) with PPII helix structure was solvated in water within a cubic simulation box, with dimensions at least 2 nm larger than the length of PPro chain. Subsequently, the system was well equilibrated in the isobaric isothermal (NPT) ensemble at 300 K. Thereafter, three different configurations of

each polyproline were randomly selected from the well equilibrated NPT-MD simulations to perform WTMetaD simulations. To probe the conformational space of PPro (DP=3,8,15), the radius of gyration (R_g) of the PPro backbone was employed as CV to bias. After thorough validation, WTMetaD simulation parameters were set as follows: Gaussian width (σ) was 0.01 nm, and the bias factor (γ) was set to 100 for all simulations. Gaussians were deposited every 500 steps with an initial height (W) of 0.6, 0.8 and 1.0 kJ/mol for P3, P8 and P15, respectively. The free energy profiles were calculated using the reweighing technique proposed by Tiwary and Parrinello,⁸⁶ with final energy profiles obtained by averaging the results of three independent simulations with different initial conformations.

Additionally, the WTMetaD simulations were conducted to examine the assembly and aggregation characteristics of PPro with varying DPs. Initially, two PPro molecules (DP=3, 8, 15) were solvated in solution containing approximately 11000 water molecules, achieving concentration of 0.01 M (~10 mg/mL) to explore the energy landscape of PPro for the dimer formation. In this context, the coordination number (CN) of the heavy atoms between two PPro molecules was used as CV to bias. Here, the CN was calculated as

$$CN = \sum_{i \in A} \sum_{j \in B} s_{ij} \quad (1)$$

where A and B represent the heavy atoms of two different PPro molecules. A larger CN value indicates a higher aggregation propensity for PPro. The s_{ij} is a switching function, which defined as

$$s_{ij} = \frac{1 - \left(\frac{r_{ij}}{r_0}\right)^n}{1 - \left(\frac{r_{ij}}{r_0}\right)^m} \quad (2)$$

where r_{ij} represents the distance between heavy atoms i and j . The cutoff distance for the contact r_0 , was set to 0.55 nm in this study. The values of n and m were set to 6 and 12, respectively, allowing for a smooth transition in the switching function. The parameters for WTMetaD simulations have been set as follows: Gaussian potentials, with $\sigma=2.0/4.0/5.0$, $\gamma=20/20/20$ and $W=1.0/1.0/1.0$ kJ/mol for P3, P8, and P15, respectively. Gaussians were deposited every 500 steps to progressively build the free energy landscape. Additionally, larger systems comprising 20 P3, 8 P8, and 4 P15 molecules were constructed to facilitate a more comprehensive investigation of the aggregation properties (multimers) of PPro, maintaining a similar mass concentration of approximately 40 mg/mL (11,000 water molecules) across all simulation systems. The CN of the heavy atoms of PPro was again selected as the CV to bias. In this context, equation (1) should be interpreted as a sum over all $N(N-1)/2$ pairs of the N heavy atoms of PPro. During the WTMetaD simulations, Gaussian potentials with $\sigma=20$, $\gamma=20$ and $W=1.0$ kJ/mol were deposited every 500 steps. The free energy profiles and their corresponding uncertainty were calculated using the reweighing technique of Tiwary and Parrinello [88], which yielded very small uncertainty values of less than 0.3 kJ/mol in our simulations.

4.3. Analysis Details. The CHILL+ algorithm⁸⁷ was employed for the identification of water molecules in ice (in both the cubic and hexagonal phases) or liquid phase. To accurately describe the advancing ice front, ice molecules (identified by CHILL+ algorithm) with fewer than three other ice molecules within 0.5 nm were also considered as liquid water. After that, interfacial water molecules located within 0.35 nm of either cubic or hexagonal ice were identified as belonging to the ice phase. To estimate the number of -CH₂ groups attached to the ice surface, the -CH₂ groups were treated as attached to the ice surface if there are six ice molecules (a hexatomic ring) within 5.5 Å (the

first solvation shell) of it. The hydrogen bonds were identified with a donor-acceptor distance of less than 3.5 Å and a hydrogen-donor-acceptor angle of less than 30°. ⁸⁸ Moreover, the PPII helix was identified based on the backbone dihedral angles $\phi \in [-110, -30]$ and $\psi \in [120, 180]$. ⁷² The embedded depth of PPro on the ice surface was estimated by the $z_{PPro} - z_{Ice}$, where z_{PPro} represents the lowest point of the protein and z_{Ice} denotes the position of ice surface along the in z-axis. All the PPro molecules that were bound to the ice but not overgrown by the advancing ice front in simulations were counted. The coverage area of PPro chains on the ice surface was determined by projecting the heavy atom positions of the polymer bound to the ice onto the xy-plane, using an atomic radius of 0.5 nm. Additionally, the interaction energies, including electrostatic and van der Waals interactions, were analyzed to assess the interactions between PPro and water/PPro during ice growth inhibition simulations. The Visual Molecular Dynamics (VMD) package was used for visualization purposes. ⁸⁹

ASSOCIATED CONTENT

Supporting Information.

Representation of the ice growth inhibition simulation system. Embedded states of PPro molecules on the ice surface. Engulfment states of P3, P8L, and P15L by ice. Gibbs free energy (ΔG) profile as a function of the coordination number (CN) at a low concentration (~10 mg/mL). Representative configurations of metastable states of P8 and P15 in the metadynamics simulations at a high concentration (~40 mg/mL). Total number of hydrogen bonds between P15 molecules as a function of CN in the metadynamics simulation at high concentration.

Movies S1-S5 describing the impact of P3, P8L, P8C, P15L, P15C on ice growth at 265 K, respectively (MP4)

AUTHOR INFORMATION

Corresponding Author

* Zhaoru Sun - School of Physical Science and Technology, ShanghaiTech University, Shanghai 201210, China

Email: sunzhr@shanghaitech.edu.cn

Author Contributions

W.Y. and Z.S. designed research; W.Y. and Y.L. performed research and analyzed; W.Y. and Z.S. wrote the paper. All authors have read and agreed to the published version of the manuscript.

Funding Sources

The authors gratefully acknowledge the financial support from the National Natural Science Foundation of China (12104306), Shanghai Tech start-up funding, and the Double First-Class Initiative Fund of ShanghaiTech University (SYLDX0342022).

Notes

The authors declare no competing financial interest.

ACKNOWLEDGMENT

The authors gratefully acknowledge the financial support from the National Natural Science Foundation of China (12104306) and the Double First-Class Initiative Fund of ShanghaiTech University (SYLDX0342022). We also thank the computing resources and technical support provided by the High-Performance Computing (HPC) Platform at ShanghaiTech University.

REFERENCE

- (1) T. Chang and G. Zhao Ice inhibition for cryopreservation: materials, strategies, and challenges. *Adv. Sci.* **2021**, *8*, 2002425.
- (2) C. Polge, A. U. Smith and A. S. Parkes Revival of spermatozoa after vitrification and dehydration at low temperatures. *Nature* **1949**, *164*, 666-666.

- (3) P. Mazur Cryobiology: The Freezing of Biological Systems: The responses of living cells to ice formation are of theoretical interest and practical concern. *Science* **1970**, *168*, 939-949.
- (4) W. F. Rall and G. M. Fahy Ice-free cryopreservation of mouse embryos at $-196\text{ }^{\circ}\text{C}$ by vitrification. *Nature* **1985**, *313*, 573-575.
- (5) R. C. Deller, M. Vatish, D. A. Mitchell and M. I. Gibson Synthetic polymers enable non-vitreous cellular cryopreservation by reducing ice crystal growth during thawing. *Nat. Commun.* **2014**, *5*, 3244.
- (6) J. F. Carpenter and T. N. Hansen Antifreeze protein modulates cell survival during cryopreservation: mediation through influence on ice crystal growth. *Proc. Natl. Acad. Sci. U.S.A.* **1992**, *89*, 8953-8957.
- (7) M. Dou, C. Lu and W. Rao Bioinspired materials and technology for advanced cryopreservation. *Trends. Biotechnol.* **2022**, *40*, 93-106.
- (8) A. Murray, T. R. Congdon, R. M. Tomás, P. Kilbride and M. I. Gibson Red blood cell cryopreservation with minimal post-thaw lysis enabled by a synergistic combination of a cryoprotecting polyampholyte with DMSO/trehalose. *Biomacromolecules* **2021**, *23*, 467-477.
- (9) M. D. Ekpo, J. Xie, Y. Hu, X. Liu, F. Liu, J. Xiang, R. Zhao, B. Wang and S. Tan Antifreeze proteins: Novel applications and navigation towards their clinical application in cryobanking. *Int. J. Mol. Sci.* **2022**, *23*, 2639.
- (10) L. F. Correia, B. R. Alves, R. I. Batista, P. Merrimillod and J. M. Souza-Fabjan Antifreeze proteins for low-temperature preservation in reproductive medicine: a systematic review over the last three decades. *Theriogenology* **2021**, *176*, 94-103.
- (11) I. M. Lifshitz and V. V. Slyozov The kinetics of precipitation from supersaturated solid solutions. *J. Phys. Chem. Solids.* **1961**, *19*, 35-50.
- (12) C. Budke, C. Heggemann, M. Koch, N. Sewald and T. Koop Ice recrystallization kinetics in the presence of synthetic antifreeze glycoprotein analogues using the framework of LSW theory. *J. Phys. Chem. B* **2009**, *113*, 2865-2873.
- (13) T. Congdon, R. Notman and M. I. Gibson Antifreeze (glyco) protein mimetic behavior of poly (vinyl alcohol): detailed structure ice recrystallization inhibition activity study. *Biomacromolecules* **2013**, *14*, 1578-1586.
- (14) P. Mazur Freezing of living cells: mechanisms and implications. *Am. J. Physiol. Cell Physiol.* **1984**, *247*, C125-C142.
- (15) K. A. Murray and M. I. Gibson Chemical approaches to cryopreservation. *Nat. Rev. Chem.* **2022**, *6*, 579-593.
- (16) C. Budke, A. Dreyer, J. Jaeger, K. Gimpel, T. Berkemeier, A. S. Bonin, L. Nagel, C. Plattner, A. L. DeVries and N. Sewald Quantitative efficacy classification of ice recrystallization inhibition agents. *Cryst. Growth. & Des.* **2014**, *14*, 4285-4294.
- (17) Z. Liu, X. Zheng and J. Wang Bioinspired ice-binding materials for tissue and organ cryopreservation. *J. Am. Chem. Soc.* **2022**, *144*, 5685-5701.
- (18) J. A. Raymond and A. L. DeVries Adsorption inhibition as a mechanism of freezing resistance in polar fishes. *Proc. Natl. Acad. Sci. U.S.A.* **1977**, *74*, 2589-2593.
- (19) C. Knight, E. Driggers and A. DeVries Adsorption to ice of fish antifreeze glycopeptides 7 and 8. *Biophys. J.* **1993**, *64*, 252-259.
- (20) M. T. Warren, I. Galpin, F. Bachtiger, M. I. Gibson and G. C. Sosso Ice recrystallization inhibition by amino acids: The curious case of alpha-and beta-alanine. *J. Phys. Chem. Lett.* **2022**, *13*, 2237-2244.
- (21) S. Zepeda, E. Yokoyama, Y. Uda, C. Katagiri and Y. Furukawa In situ observation of antifreeze glycoprotein kinetics at the ice interface reveals a two-step reversible adsorption mechanism. *Cryst. Growth. Des.* **2008**, *8*, 3666-3672.
- (22) Z. Ding, C. Wang, B. Zhou, M. Su, S. Yang, Y. Li, C. Qu and H. Liu Antifreezing hydroxyl monolayer of small molecules on a nanogold surface. *Nano Lett.* **2022**, *22*, 5307-5315.
- (23) X. Sun, R. Guo, T. Zhan, Y. Kou, X. Ma, H. Song, W. Zhou, L. Song, H. Zhang and F. Xie Retarding ice recrystallization by tamarind seed polysaccharide: Investigation in ice cream mixes and insights from molecular dynamics simulation. *Food Hydrocoll.* **2024**, *149*, 109579.
- (24) A. A. Burkey, C. L. Riley, L. K. Wang, T. A. Hatridge and N. A. Lynd Understanding poly (vinyl alcohol)-mediated ice recrystallization inhibition through ice adsorption measurement and pH effects. *Biomacromolecules* **2018**, *19*, 248-255.
- (25) L. L. Olijve, K. Meister, A. L. DeVries, J. G. Duman, S. Guo, H. J. Bakker and I. K. Voets Blocking rapid ice crystal growth through nonbasal plane adsorption of antifreeze proteins. *Proc. Natl. Acad. Sci. U.S.A.* **2016**, *113*, 3740-3745.
- (26) M. Li, C. R. Luckett and T. Wu Potent time-dependent ice recrystallization inhibition activity of cellulose nanocrystals in sucrose solutions. *Biomacromolecules* **2021**, *23*, 497-504.
- (27) J. Yang, M. Liu, T. Zhang, J. Ma, Y. Ma, S. Tian, R. Li, Y. Han and L. Zhang Cell-friendly regulation of ice crystals by antifreeze organism-inspired materials. *AIChE J.* **2022**, *68*, e17822.
- (28) L. Weng, S. L. Stott and M. Toner Molecular dynamics at the interface between ice and poly (vinyl alcohol) and ice recrystallization inhibition. *Langmuir* **2017**, *34*, 5116-5123.
- (29) W. Yang, Y. Liao, Q. Shi and Z. Sun The Atomistic Understanding of the Ice Recrystallization Inhibition Activity of Antifreeze Glycoproteins. *Crystals* **2023**, *13*, 405.
- (30) Z. Wang, M. Li and T. Wu Ice recrystallization inhibition activity in bile salts. *J. Colloid Interface Sci.* **2023**, *629*, 728-738.
- (31) C. I. Biggs, T. L. Bailey, B. Graham, C. Stubbs, A. Fayter and M. I. Gibson Polymer mimics of biomacromolecular antifreezes. *Nat. Commun.* **2017**, *8*, 1546.
- (32) T. R. Congdon, R. Notman and M. I. Gibson Influence of block copolymerization on the antifreeze protein mimetic ice recrystallization inhibition activity of poly (vinyl alcohol). *Biomacromolecules* **2016**, *17*, 3033-3039.
- (33) B. Graham, T. L. Bailey, J. R. Healey, M. Marcellini, S. Deville and M. I. Gibson Polyproline as a minimal antifreeze protein mimic that enhances the cryopreservation of cell monolayers. *Angew. Chem. Int. Ed. Engl.* **2017**, *56*, 15941-15944.
- (34) S. Park, Z. Piao, J. K. Park, H. J. Lee and B. Jeong Ice Recrystallization Inhibition Using l-Alanine/l-Lysine Copolymers. *ACS Applied Polymer Materials* **2022**, *4*, 2896-2907.
- (35) S. Y. Lee, M. Kim, T. K. Won, S. H. Back, Y. Hong, B.-S. Kim and D. J. Ahn Janus regulation of ice growth by hyperbranched polyglycerols generating dynamic hydrogen bonding. *Nat. Commun.* **2022**, *13*, 6532.
- (36) P. I. Sepulveda-Medina, C. Wang, R. Li, M. Fukuto and B. D. Vogt Influence of the Nature of Aliphatic Hydrophobic Physical Crosslinks on Water Crystallization in Copolymer Hydrogels. *J. Phys. Chem. B* **2022**, *126*, 5544-5554.

- (37) P. G. Georgiou, N. L. Kinney, I. Kontopoulou, A. N. Baker, S. A. Hindmarsh, A. Bissoyi, T. R. Congdon, T. F. Whale and M. I. Gibson Poly (vinyl alcohol) molecular bottlebrushes nucleate ice. *Biomacromolecules* **2022**, *23*, 5285-5296.
- (38) E. A. Delesky, L. F. Garcia, A. J. Lobo, R. A. Mikofsky, N. D. Dowdy, J. D. Wallat, G. M. Miyake and W. V. Srubar III Bioinspired threonine-based polymers with potent ice recrystallization inhibition activity. *ACS Appl. Polym. Mater.* **2022**, *4*, 7934-7942.
- (39) Z. Piao, M. Patel, J. K. Park and B. Jeong Poly (l-alanine-co-l-lysine)-g-trehalose as a biomimetic cryoprotectant for stem cells. *Biomacromolecules* **2022**, *23*, 1995-2006.
- (40) J. K. Park, S.-J. Park and B. Jeong Poly (l-alanine-co-l-threonine succinate) as a Biomimetic Cryoprotectant. *ACS Appl. Mater.* **2023**, *15*, 58092-58102.
- (41) P. M. Naullage and V. Molinero Slow propagation of ice binding limits the ice-recrystallization inhibition efficiency of PVA and other flexible polymers. *J. Am. Chem. Soc.* **2020**, *142*, 4356-4366.
- (42) D. E. Mitchell, N. R. Cameron and M. I. Gibson Rational, yet simple, design and synthesis of an antifreeze-protein inspired polymer for cellular cryopreservation. *Chem. Commun.* **2015**, *51*, 12977-12980.
- (43) Y. Gao, H. Qi and L. Zhang Advances in Antifreeze Molecules: From Design and Mechanisms to Applications. *Industrial & Engineering Chemistry Research* **2023**, *62*, 7839-7858.
- (44) X. Sun, R. Guo, Y. Kou, H. Song, T. Zhan, J. Wu, L. Song, H. Zhang, F. Xie and J. Wang Inhibition of ice recrystallization by tamarind (*Tamarindus indica* L.) seed polysaccharide and molecular weight effects. *Carbohydr. Polym.* **2023**, *301*, 120358.
- (45) A. K. Balcerzak, M. Febraro and R. N. Ben The importance of hydrophobic moieties in ice recrystallization inhibitors. *RSC Adv.* **2013**, *3*, 3232-3236.
- (46) T. Li, M. Li, Q. Zhong and T. Wu Effect of fibril length on the ice recrystallization inhibition activity of nanocelluloses. *Carbohydr. Polym.* **2020**, *240*, 116275.
- (47) W. Hua, Y. Wang, C.-Y. Guo, J. Wang, S. Li and L. Guo Ice recrystallization inhibition activity of protein mimetic peptoids. *J Inorg Organomet Polym* **2021**, *31*, 203-208.
- (48) Y. Tachibana, G. L. Fletcher, N. Fujitani, S. Tsuda, K. Monde and S. I. Nishimura Antifreeze glycoproteins: elucidation of the structural motifs that are essential for antifreeze activity. *Angew. Chem.* **2004**, *116*, 874-880.
- (49) M. I. Gibson, C. A. Barker, S. G. Spain, L. Albertin and N. R. Cameron Inhibition of ice crystal growth by synthetic glycopolymers: implications for the rational design of antifreeze glycoprotein mimics. *Biomacromolecules* **2009**, *10*, 328-333.
- (50) M. Hachisu, H. Hinou, M. Takamichi, S. Tsuda, S. Koshida and S.-I. Nishimura One-pot synthesis of cyclic antifreeze glycopeptides. *Chem. Commun.* **2009**, 1641-1643.
- (51) F. Bachtiger, T. R. Congdon, C. Stubbs, M. I. Gibson and G. C. Sosso The atomistic details of the ice recrystallisation inhibition activity of PVA. *Nat. Commun.* **2021**, *12*, 1323.
- (52) Q. Qin, L. Zhao, Z. Liu, T. Liu, J. Qu, X. Zhang, R. Li, L. Yan, J. Yan and S. Jin Bioinspired l-proline oligomers for the cryopreservation of oocytes via controlling ice growth. *ACS Appl. Mater.* **2020**, *12*, 18352-18362.
- (53) Y. Chen, X. Sui, T. Zhang, J. Yang, L. Zhang and Y. Han Ice recrystallization inhibition mechanism of zwitterionic poly (carboxybetaine methacrylate). *Phys. Chem. Chem. Phys.* **2023**, *25*, 2752-2757.
- (54) S. Kim, J. K. Park, S.-J. Park and B. Jeong Oligonucleotides as Inhibitors of Ice Recrystallization. *Biomacromolecules* **2023**, *24*, 2118-2126.
- (55) L. Han, H. Wang, W. Cai and X. Shao Mechanism of Binding of Polyproline to Ice via Interfacial Water: An Experimental and Theoretical Study. *J. Phys. Chem. Lett.* **2023**, *14*, 4127-4133.
- (56) R. Rojas, M. Aróstica, P. Carvajal-Rondanelli, F. Albericio, F. Guzmán and C. Cárdenas Relationship between type II polyproline helix secondary structure and thermal hysteresis activity of short homopeptides. *Electronic Journal of Biotechnology* **2022**, *59*, 62-73.
- (57) N. Judge, P. G. Georgiou, A. Bissoyi, A. Ahmad, A. Heise and M. I. Gibson High molecular weight polyproline as a potential biosourced ice growth inhibitor: synthesis, ice recrystallization inhibition, and specific ice face binding. *Biomacromolecules* **2023**, *24*, 2459-2468.
- (58) R. Drori, C. Li, C. Hu, P. Raiteri, A. L. Rohl, M. D. Ward and B. Kahr A supramolecular ice growth inhibitor. *J. Am. Chem. Soc.* **2016**, *138*, 13396-13401.
- (59) Y. D. Kim, W. H. Jung, D. J. Ahn and D.-K. Lim Self-Assembled Nanostructures of Homo-Oligopeptide as a Potent Ice Growth Inhibitor. *Nano Letters* **2023**, *23*, 9500-9507.
- (60) R. Suris-Valls, T. P. Hogervorst, S. M. Schoenmakers, M. M. Hendrix, L. Milroy and I. K. Voets Inhibition of ice recrystallization by nanotube-forming cyclic peptides. *Biomacromolecules* **2022**, *23*, 520-529.
- (61) B. Xue, L. Zhao, X. Qin, M. Qin, J. Lai, W. Huang, H. Lei, J. Wang, W. Wang and Y. Li Bioinspired ice growth inhibitors based on self-assembling peptides. *ACS Macro Lett.* **2019**, *8*, 1383-1390.
- (62) S. Jin, L. Yin, B. Kong, S. Wu, Z. He, H. Xue, Z. Liu, Q. Cheng, X. Zhou and J. Wang Spreading fully at the ice-water interface is required for high ice recrystallization inhibition activity. *Sci. China Chem.* **2019**, *62*, 909-915.
- (63) T. Li, M. Li, V. P. Dia, S. Lenaghan, Q. Zhong and T. Wu Electrosterically stabilized cellulose nanocrystals demonstrate ice recrystallization inhibition and cryoprotection activities. *Int. J. Biol. Macromol.* **2020**, *165*, 2378-2386.
- (64) T. Li, Y. Zhao, Q. Zhong and T. Wu Inhibiting ice recrystallization by nanocelluloses. *Biomacromolecules* **2019**, *20*, 1667-1674.
- (65) B. Grishkovskii, T. Khromova and L. IuA Aggregation of poly-L-proline in aqueous solution. *Mol. Biol.* **1981**, *15*, 310-315.
- (66) C. A. Swenson and R. Formanek Infrared study of poly-L-proline in aqueous solution. *J. Phys. Chem.* **1967**, *71*, 4073-4077.
- (67) P. Pandey and S. S. Mallajosyula Elucidating the role of key structural motifs in antifreeze glycoproteins. *Phys. Chem. Chem. Phys.* **2019**, *21*, 3903-3917.
- (68) S. Doose, H. Neuweiler, H. Barsch and M. Sauer Probing polyproline structure and dynamics by photoinduced electron transfer provides evidence for deviations from a regular polyproline type II helix. *Proc. Natl. Acad. Sci. U.S.A.* **2007**, *104*, 17400-17405.
- (69) L. Garbuio, B. Lewandowski, P. Wilhelm, L. Ziegler, M. Yulikov, H. Wennemers and G. Jeschke Shape persistence of polyproline II helical oligoproline. *Chem. Eur. J.* **2015**, *21*, 10747-10753.

- (70) M. Chasnitsky and I. Braslavsky Ice-binding proteins and the applicability and limitations of the kinetic pinning model. *Philosophical Transactions of the Royal Society A: Mathematical, Physical and Engineering Sciences* **2019**, *377*, 20180391.
- (71) L. M. Sander and A. V. Tkachenko Kinetic Pinning and Biological Antifreezes. *Phys. Rev. Lett.* **2004**, *93*, 128102.
- (72) K. Mochizuki and V. Molinero Antifreeze glycoproteins bind reversibly to ice via hydrophobic groups. *J. Am. Chem. Soc.* **2018**, *140*, 4803-4811.
- (73) M. J. Abraham, T. Murtola, R. Schulz, S. Páll, J. C. Smith, B. Hess and E. Lindahl GROMACS: High performance molecular simulations through multi-level parallelism from laptops to supercomputers. *SoftwareX* **2015**, *1*, 19-25.
- (74) R. B. Best, X. Zhu, J. Shim, P. E. M. Lopes, J. Mittal, M. Feig and A. D. MacKerell, Jr. Optimization of the Additive CHARMM All-Atom Protein Force Field Targeting Improved Sampling of the Backbone ϕ , ψ and Side-Chain χ_1 and χ_2 Dihedral Angles. *J. Chem. Theory Comput.* **2012**, *8*, 3257-3273.
- (75) J. Abascal, E. Sanz, R. García Fernández and C. Vega A potential model for the study of ices and amorphous water: TIP4P/Ice. *J. Chem. Phys.* **2005**, *122*,
- (76) R. García Fernández, J. L. Abascal and C. Vega The melting point of ice Ih for common water models calculated from direct coexistence of the solid-liquid interface. *J. Chem. Phys.* **2006**, *124*,
- (77) T. Darden, D. York and L. Pedersen Particle mesh Ewald: An $N \cdot \log(N)$ method for Ewald sums in large systems. *J. Chem. Phys.* **1993**, *98*, 10089-10092.
- (78) B. Hess, H. Bekker, H. J. Berendsen and J. G. Fraaije LINCS: a linear constraint solver for molecular simulations. *J. Comput. Chem.* **1997**, *18*, 1463-1472.
- (79) S. Nosé A unified formulation of the constant temperature molecular dynamics methods. *J. Chem. Phys.* **1984**, *81*, 511-519.
- (80) W. G. Hoover Canonical dynamics: Equilibrium phase-space distributions. *Phys. Rev. A* **1985**, *31*, 1695.
- (81) M. Parrinello and A. Rahman Polymorphic transitions in single crystals: A new molecular dynamics method. *J. Appl. Phys.* **1981**, *52*, 7182-7190.
- (82)
- (83) A. Barducci, G. Bussi and M. Parrinello Well-tempered metadynamics: a smoothly converging and tunable free-energy method. *Phys. Rev. Lett.* **2008**, *100*, 020603.
- (84) G. A. Tribello, M. Bonomi, D. Branduardi, C. Camilloni and G. Bussi PLUMED 2: New feathers for an old bird. *Comput. Phys. Commun.* **2014**, *185*, 604-613.
- (85) M. Bonomi, G. Bussi, C. Camilloni, G. A. Tribello, P. Banáš, A. Barducci, M. Bernetti, P. G. Bolhuis, S. Bottaro, D. Branduardi, R. Capelli, P. Carloni, M. Ceriotti, A. Cesari, H. Chen, W. Chen, F. Colizzi, S. De, M. De La Pierre, D. Donadio, V. Drobot, B. Ensing, A. L. Ferguson, M. Filizola, J. S. Fraser, H. Fu, P. Gasparotto, F. L. Gervasio, F. Giberti, A. Gil-Ley, T. Giorgino, G. T. Heller, G. M. Hocky, M. Iannuzzi, M. Invernizzi, K. E. Jelfs, A. Jussupow, E. Kirilin, A. Laio, V. Limongelli, K. Lindorff-Larsen, T. Löhr, F. Marinelli, L. Martin-Samos, M. Masetti, R. Meyer, A. Michaelides, C. Molteni, T. Morishita, M. Nava, C. Paissoni, E. Papaleo, M. Parrinello, J. Pfendtner, P. Piaggi, G. Piccini, A. Pietropaolo, F. Pietrucci, S. Pipolo, D. Provasi, D. Quigley, P. Raiteri, S. Raniolo, J. Rydzewski, M. Salvalaglio, G. C. Sosso, V. Spiwok, J. Šponer, D. W. H. Swenson, P. Tiwary, O. Valsson, M. Vendruscolo, G. A. Voth, A. White and T. P. consortium Promoting transparency and reproducibility in enhanced molecular simulations. *Nat. Methods* **2019**, *16*, 670-673.
- (86) P. Tiwary and M. Parrinello A time-independent free energy estimator for metadynamics. *J. Phys. Chem. B* **2015**, *119*, 736-742.
- (87) A. H. Nguyen and V. Molinero Identification of clathrate hydrates, hexagonal ice, cubic ice, and liquid water in simulations: The CHILL+ algorithm. *J. Phys. Chem. B* **2015**, *119*, 9369-9376.
- (88) H. Xu and B. Berne Hydrogen-bond kinetics in the solvation shell of a polypeptide. *J. Phys. Chem. B* **2001**, *105*, 11929-11932.
- (89) W. Humphrey, A. Dalke and K. Schulten VMD: visual molecular dynamics. *J. Mol. Graph.* **1996**, *14*, 33-38.

Revealing Molecular Mechanism of Nonmonotonic Relationship between Antifreeze Activity and Chain Length in Polyprolines

Wentao Yang, Yucong Liao, Zhaoru Sun*

School of Physical Science and Technology, ShanghaiTech University, Shanghai 201210, China

* Corresponding Author

E-mail address: sunzhr@shanghaitech.edu.cn (Z. S.)

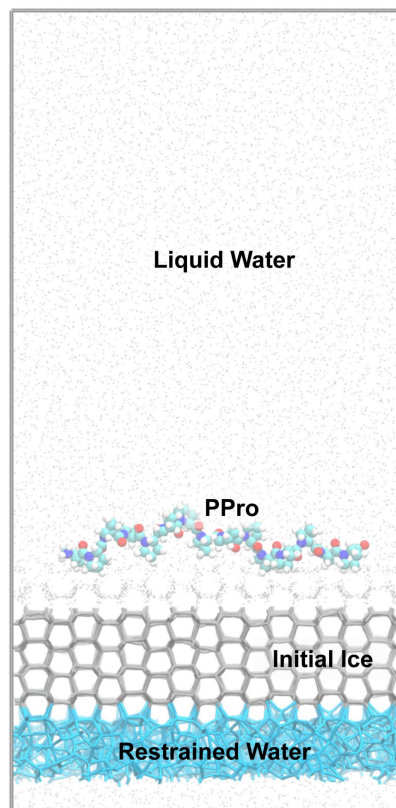


Figure S1. Representation of the ice growth inhibition simulation system. Four layers of initial ice (colored gray) are restrained by a harmonic potential, with the primary prismatic face oriented toward the water phases. The oxygen atoms of liquid water molecules are represented as gray points. A 1 nm thick water layer (colored cyan) below the hexagonal ice slab is restrained to prevent downward ice growth.

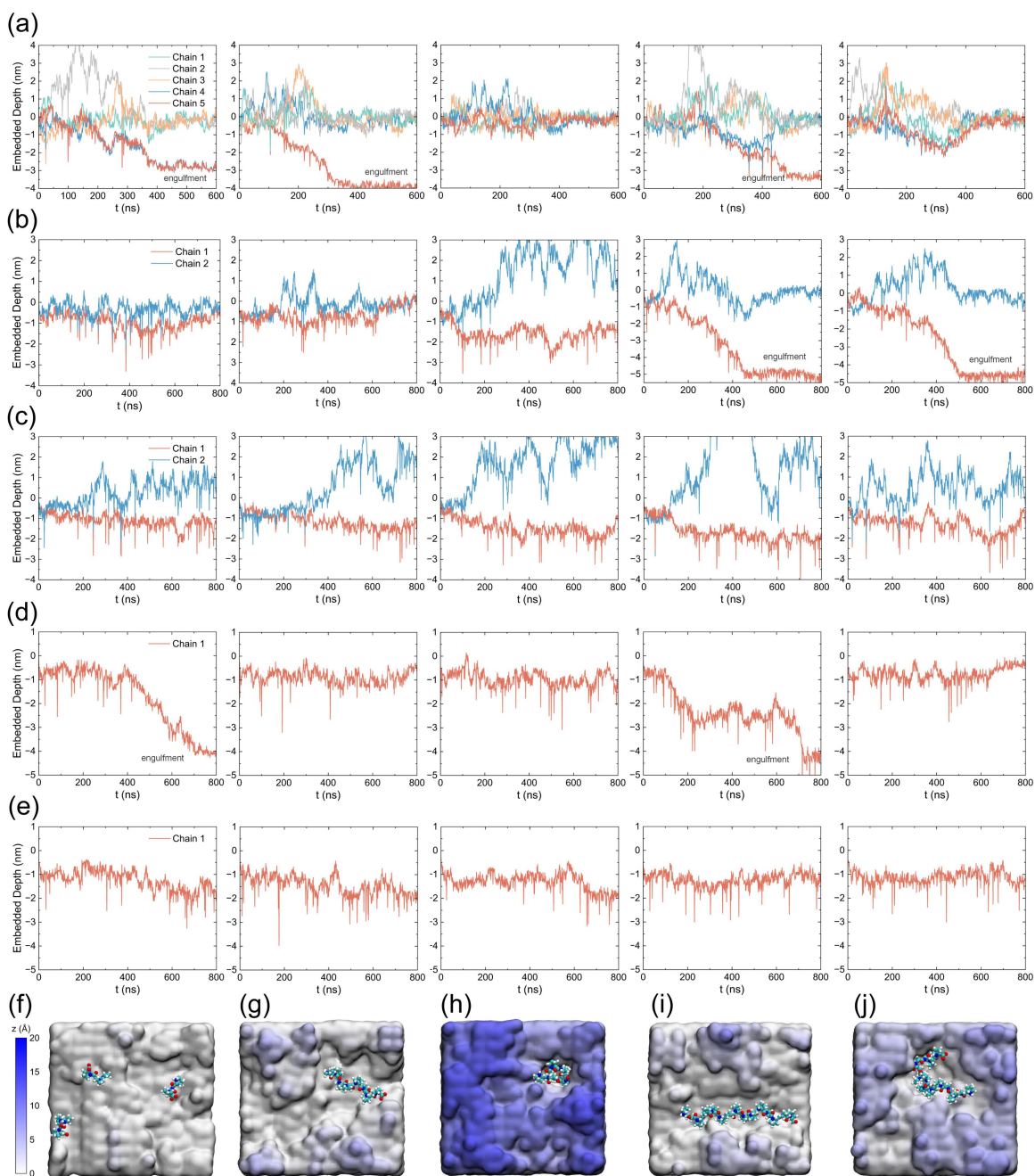


Figure S2. Embedded states of PPro molecules on the ice surface. (a-e) Embedded depth ($z_{PPro} - z_{ice}$) of P3 (a), P8L (b), P8C (c), P15L (d), and P15C (e) at the ice surface. (f-j) Representative binding states and configurations of P3 (f), P8L (g), P8C (h), P15L (i), and P15C (j), with the ice surface color-coded by the z-axis height. The bottom atom of each PPro molecule is used as the reference point ($z=0$). PPro molecules that stay away from the ice surface (un-bound) are not shown.

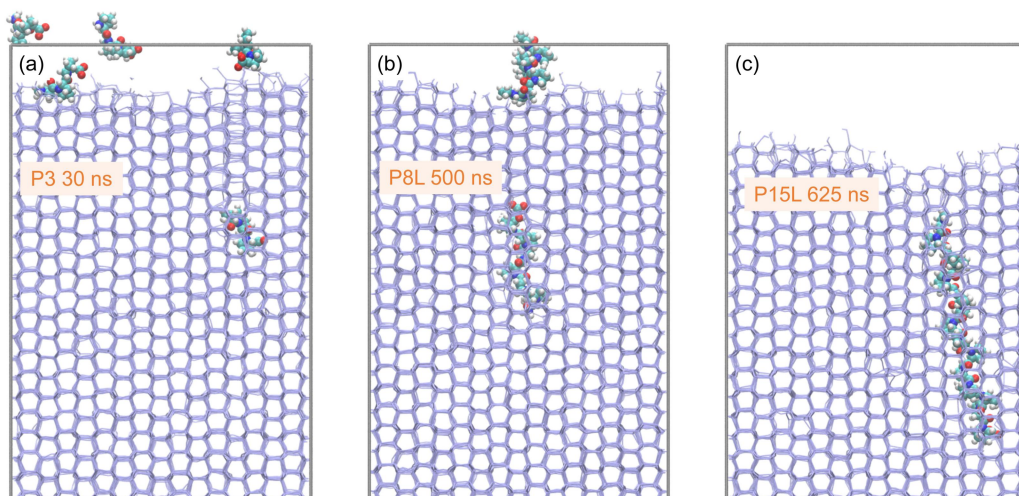


Figure S3. Representative snapshots of PPro being engulfed by ice growth. (a) P3 is too small and is easily engulfed by the growing ice front. (b) P8 and (c) P15 become engulfed by ice when aligned parallel to the growing ice front.

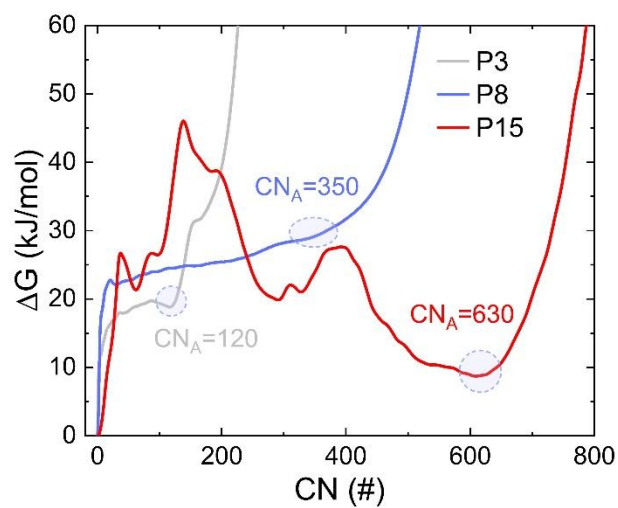


Figure S4. Gibbs free energy (ΔG) profile as a function of the coordination number (CN) at a low concentration (~ 10 mg/mL), with small uncertainty values (less than 0.3 kJ/mol) obtained from our metadynamics simulations.

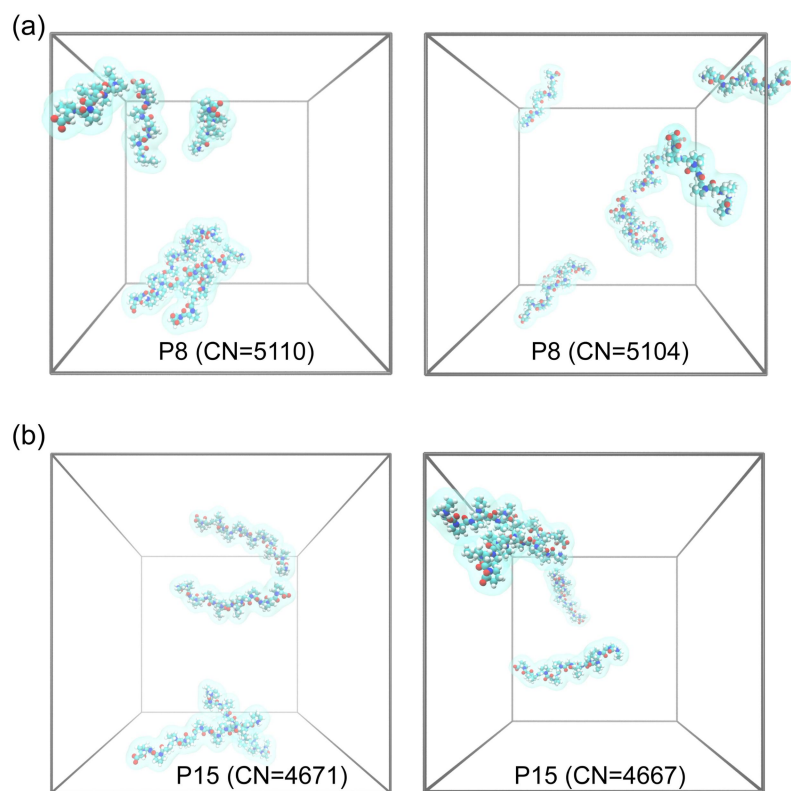


Figure S5. Representative configurations of metastable states ($CN \approx 4700$ and $CN \approx 5100$) for P8 (a) and P15 (b) in the metadynamics simulations at high concentration. These states primarily involve unstable dimer formations.

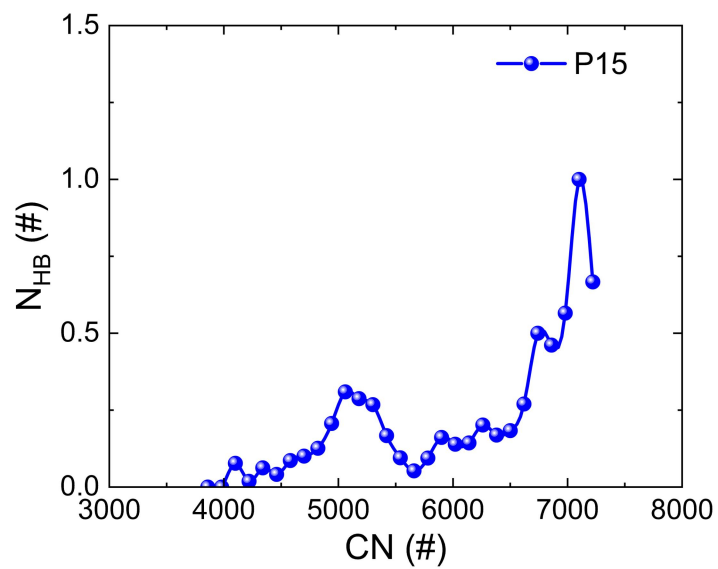


Figure S6. Total number of hydrogen bonds between P15 molecules as a function of coordination number (CN) in the metadynamics simulation at high concentration. The results show that almost no intermolecular hydrogen bonds are formed within P15 aggregations.